

Chandra and Magellan/FIRE follow-up observations of PSO167–13: an X-ray weak QSO at $z = 6.515$

F. Vito^{*1,2}, W. N. Brandt^{3,4,5}, F. Ricci^{6,7}, E. Congiu⁸, T. Connor^{9,10}, E. Bañados¹¹, F. E. Bauer^{2,12,13}, R. Gilli⁷, B. Luo^{14,15,16}, C. Mazzucchelli¹⁷, M. Mignoli⁷, O. Shemmer¹⁸, C. Vignali^{6,7}, F. Calura⁷, A. Comastri⁷, R. Decarli⁷, S. Gallerani¹, R. Nanni¹⁹, M. Brusa^{6,7}, N. Cappelluti²⁰, F. Civano²¹, and G. Zamorani⁷

¹ Scuola Normale Superiore, Piazza dei Cavalieri 7, 56126, Pisa (Italy)

² Instituto de Astrofísica and Centro de Astroingeniería, Facultad de Física, Pontificia Universidad Católica de Chile, Casilla 306, Santiago 22, Chile

³ Department of Astronomy & Astrophysics, 525 Davey Lab, The Pennsylvania State University, University Park, PA 16802, USA

⁴ Institute for Gravitation and the Cosmos, The Pennsylvania State University, University Park, PA 16802, USA

⁵ Department of Physics, The Pennsylvania State University, University Park, PA 16802, USA

⁶ Dipartimento di Fisica e Astronomia, Università degli Studi di Bologna, via Gobetti 93/2, I-40129 Bologna, Italy

⁷ INAF – Osservatorio di Astrofisica e Scienza dello Spazio di Bologna, Via Gobetti 93/3, I-40129 Bologna, Italy

⁸ Departamento de Astronomía, Universidad de Chile, Camino del Observatorio 1515, Las Condes, Santiago, Chile

⁹ Jet Propulsion Laboratory, California Institute of Technology, 4800 Oak Grove Drive, Pasadena, CA 91109, USA

¹⁰ The Observatories of the Carnegie Institution for Science, 813 Santa Barbara St., Pasadena, CA 91101, USA

¹¹ Max Planck Institut für Astronomie, Königstuhl 17, D-69117, Heidelberg, Germany

¹² Millennium Institute of Astrophysics (MAS), Nuncio Monseñor Sótero Sanz 100, Providencia, Santiago, Chile

¹³ Space Science Institute, 4750 Walnut Street, Suite 205, Boulder, Colorado, 80301, USA

¹⁴ School of Astronomy and Space Science, Nanjing University, Nanjing 210093, PR China

¹⁵ Key Laboratory of Modern Astronomy and Astrophysics, Nanjing University, Ministry of Education, Nanjing, Jiangsu 210093, PR China

¹⁶ Collaborative Innovation Center of Modern Astronomy and Space Exploration, Nanjing 210093, PR China

¹⁷ European Southern Observatory, Alonso de Córdova 3107, Vitacura, Región Metropolitana, Chile

¹⁸ Department of Physics, University of North Texas, Denton, TX 76203, USA

¹⁹ Department of Physics, University of California, Santa Barbara, CA 93106-9530, USA

²⁰ Physics Department, University of Miami, Coral Gables, FL 33124, USA

²¹ Center for Astrophysics | Harvard & Smithsonian, 60 Garden st, Cambridge, MA 02138, USA

ABSTRACT

Context. The discovery of hundreds of quasi-stellar objects (QSOs) in the first Gyr of the Universe powered by already grown supermassive black holes (SMBHs) challenges our knowledge of SMBH formation. In particular, investigations of $z > 6$ QSOs presenting notable properties can provide unique information on the physics of fast SMBH growth in the early universe.

Aims. We present the results of follow-up observations of the $z = 6.515$ radio-quiet QSO PSO167–13, which is interacting with a close companion galaxy. The PSO167–13 system has been recently proposed to host the first heavily obscured X-ray source at high redshift. The goals of these new observations are to confirm the existence of the X-ray source and to investigate the rest-frame UV properties of the QSO.

Methods. We observed the PSO167–13 system with *Chandra*/ACIS-S (177 ks), and obtained new spectroscopic observations (7.2 h) with *Magellan*/FIRE.

Results. No significant X-ray emission is detected from the PSO167–13 system, suggesting that the obscured X-ray source previously tentatively detected was either due to a strong background fluctuation or is highly variable. The upper limit (90% confidence level) on the X-ray emission of PSO167–13 ($L_{2-10\text{keV}} < 8.3 \times 10^{43} \text{ ergs}^{-1}$) is the lowest available for a $z > 6$ QSO. The ratio between the X-ray and UV luminosity of $\alpha_{\text{ox}} < -1.95$ makes PSO167–13 a strong outlier from the $\alpha_{\text{ox}} - L_{\text{UV}}$ and $L_{\text{X}} - L_{\text{bol}}$ relations. In particular, its X-ray emission is > 6 times weaker than the expectation based on its UV luminosity. The new *Magellan*/FIRE spectrum of PSO167–13 is strongly affected by the unfavorable sky conditions, but the tentatively detected C IV and Mg II emission lines appear strongly blueshifted.

Conclusions. The most plausible explanations for the X-ray weakness of PSO167–13 are intrinsic weakness or small-scale absorption by Compton-thick material. The possible strong blueshift of its emission lines hints at the presence of nuclear winds, which could be related to its X-ray weakness.

Key words. early universe - galaxies: active - galaxies: high-redshift - methods: observational - galaxies: individual (J167.6415–13.4960) - X-rays: individual (J167.6415–13.4960)

1. Introduction

In the last two decades, > 200 quasi-stellar objects (QSOs) have been discovered at $z > 6$, when the Universe was < 1 Gyr old,

* fvito.astro@gmail.com

primarily thanks to the availability of wide-field optical/NIR surveys (e.g., Bañados et al. 2016, 2018b; Matsuoka et al. 2018a; Fan et al. 2019; Reed et al. 2019; Belladitta et al. 2020; Yang et al. 2020; Wang et al. 2021b). The selection of high-redshift QSOs is based on the detection of the bright rest-frame UV nuclear continuum, with all of the currently confirmed $z > 6$ QSOs classified optically as type 1 (i.e., unobscured; but see, e.g., Matsuoka et al. 2019). Therefore, while theoretical arguments and numerical simulations (e.g., Pacucci et al. 2015; Valiante et al. 2017) usually require long periods of fast and heavily obscured mass growth onto black-hole seeds ($10^2 - 10^5 M_{\odot}$; e.g., Woods et al. 2019 and references therein) in order to explain the presence of 1 – 10 billion M_{\odot} supermassive black holes (SMBHs) at $z > 6$ (e.g., Wu et al. 2015), very little is known about the population of obscured accreting SMBHs in the early universe from an observational point of view.

The accumulation of multiwavelength data for a continuously increasing number of optically selected high-redshift QSOs has recently made possible the first statistical studies of QSOs in the early universe. These new data and analyses have improved our understanding of the mechanisms of SMBH formation and early growth, their interplay with their host galaxies, their environments, and the physics of reionization (e.g., Decarli et al. 2018; Davies et al. 2019; Farina et al. 2019; Mazzucchelli et al. 2019; Neeleman et al. 2019; Onoue et al. 2019; Eilers et al. 2020; Schindler et al. 2020; Wang et al. 2021a). One of the key results is that the observable spectral energy distribution properties of high-redshift QSOs do not appear to differ strongly from their counterparts at later cosmic times, in particular concerning the UV and X-ray emission, that trace the accretion physics close to the accreting SMBHs (e.g., De Rosa et al. 2014; Gallerani et al. 2017; Mazzucchelli et al. 2017; Nanni et al. 2017; Vito et al. 2019a). However, recent results do point toward a larger fraction of weak-line QSOs (WLQs; Shen et al. 2019) and larger blueshifts of high-ionization UV emission lines at $z > 6$ (Meyer et al. 2019; Schindler et al. 2020), suggesting a high incidence of nuclear winds in these systems.

In addition to statistical sample studies, a few high-redshift QSOs have been the targets of more focused investigations into their properties (e.g., Eilers et al. 2018; Connor et al. 2019, 2020; Fan et al. 2019; Nanni et al. 2018; Mignoli et al. 2020; Spingola et al. 2020; Wang et al. 2021b). In Vito et al. (2019b), we discussed the peculiar X-ray properties of PSO J167.6415–13.4960 (hereafter PSO167–13; RA_{ICRS}=11:10:33.963, DEC_{ICRS}=−13:29:45.73; Venemans et al. 2015, 2020), a type 1 QSO at $z = 6.515$ (systemic redshift derived from the [C II] 158 μm emission line; Decarli et al. 2018). The UV luminosity of PSO167–13 ($M_{1450 \text{ \AA}} = -25.6$) places this QSO close to the break of the UV luminosity function of $z > 6$ QSOs (e.g. Jiang et al. 2016; Matsuoka et al. 2018b). Atacama Large Millimeter/submillimeter Array (ALMA) imaging revealed that PSO167–13 is interacting with a companion galaxy at a projected distance of $\approx 0.9''$ (i.e., ≈ 5 physical kpc at $z = 6.515$) and $\Delta v \approx -140 \text{ km s}^{-1}$ (i.e., $\Delta z \approx -0.004$) in velocity space (Willott et al. 2017; Neeleman et al. 2019). Companion galaxies detected with ALMA have been found for a significant fraction of high-redshift QSOs (Decarli et al. 2018; Venemans et al. 2020). The PSO167–13 system is one of only two cases in which the companion galaxy has been detected in the rest-frame UV via deep *Hubble* Space Telescope (*HST*) imaging (Decarli et al. 2019; Mazzucchelli et al. 2019).

A 59 ks *Chandra* observation of PSO167–13 revealed no counts in the 0.5–2 keV band, and three counts in the 2–5 keV band (Vito et al. 2019a,b). Due to the low background level and

excellent ($\approx 0.5''$) PSF of *Chandra*, the three counts represented a relatively significant (99.96% confidence level) detection. The lack of a soft-band counterpart suggested that the X-ray source was heavily obscured. Although the position of the X-ray source suggested an association with the companion galaxy (with a spatial offset of $\approx 0.1''$, to be compared with an offset of $\approx 1''$ from the QSO), due to the close separation of the QSO-companion system, and the positional uncertainty of the X-ray emission, we could not associate it unambiguously to one of the two galaxies.

Irrespective of the lack of a secure identification of the X-ray source with either of the two ALMA-detected galaxies, the optically selected QSO was not detected in the soft X-ray band, either because of obscuration or intrinsic faintness. X-ray weakness (i.e., X-ray emission fainter than the expectation based on known relations with the UV or bolometric luminosity) is often found in notable classes of optically classified type-1 QSOs, such as broad absorption line QSOs (BAL QSOs; e.g., Luo et al. 2014, Vito et al. 2018a), WLQs (e.g., Luo et al. 2015; Ni et al. 2018), and “red” QSOs (e.g., Pu et al. 2020). The available rest-frame UV spectrum of PSO167–13 (Venemans et al. 2015, 0.73h *VLT/FORS2* using a $1.3''$ slit, + 3.33h *Magellan/FIRE*, using a $0.6''$ slit) does not allow us classify it securely as a BAL QSO or a WLQ. However, the C IV (1549 \AA) emission line appears weak and blueshifted relative to the systemic redshift, as is often found for WLQs (e.g., Ni et al. 2018, and references therein) and, in particular, $z > 6$ QSOs (e.g., Schindler et al. 2020). Moreover, the noisy spectrum blueward of the C IV and Si IV emission lines could hide possible absorption features, characteristic of BAL QSOs. With so many uncertainties in the nature of this system, deeper X-ray and rest-frame UV observations are needed.

Here we present new *Chandra* X-ray observations and *Magellan* Folded-port InfraRed Echellette (FIRE; Simcoe et al. 2008) rest-frame UV spectroscopy of PSO167–13. The goals of these observations are to confirm the presence of an obscured X-ray source in the PSO167–13 system, constrain the level of X-ray weakness of the QSO, and investigate its possible BALQSO or WLQ nature. Errors are reported at 68% confidence levels, while limits are given at 90% confidence levels, unless otherwise noted. We adopt a flat cosmology with $H_0 = 67.7 \text{ km s}^{-1}$ and $\Omega_m = 0.307$ (Planck Collaboration et al. 2016). At $z = 6.515$, $1''$ corresponds to a physical distance of 5.6 kpc.

2. Observations and data analysis

In this section we briefly describe the *Chandra* and *Magellan*/FIRE observations of PSO167–13, and their reduction.

2.1. *Chandra* observations

In Cycle 21, we observed PSO167–13 with *Chandra* ACIS-S (S3 chip) for 117.4 ks. Considering also the 59.3 ks dataset taken in 2018 (Vito et al. 2019b), the total *Chandra* coverage of PSO167–13 is ≈ 177 ks (see Tab. 1 for a summary of the X-ray pointings). We reprocessed the *Chandra* observations with the *chandra_repro* script in CIAO 4.12 (Fruscione et al. 2006),¹ using CALDB v4.9.3,² setting the option *check_vf_pha=yes* in the case of observations taken in Very Faint mode.

In order to correct the astrometry of each observation, we performed source detection with the *wavdetect* script with a non-source probability threshold of 10^{-6} on each individual *Chandra*

¹ <http://cxc.harvard.edu/ciao/>

² <http://cxc.harvard.edu/caldb/>

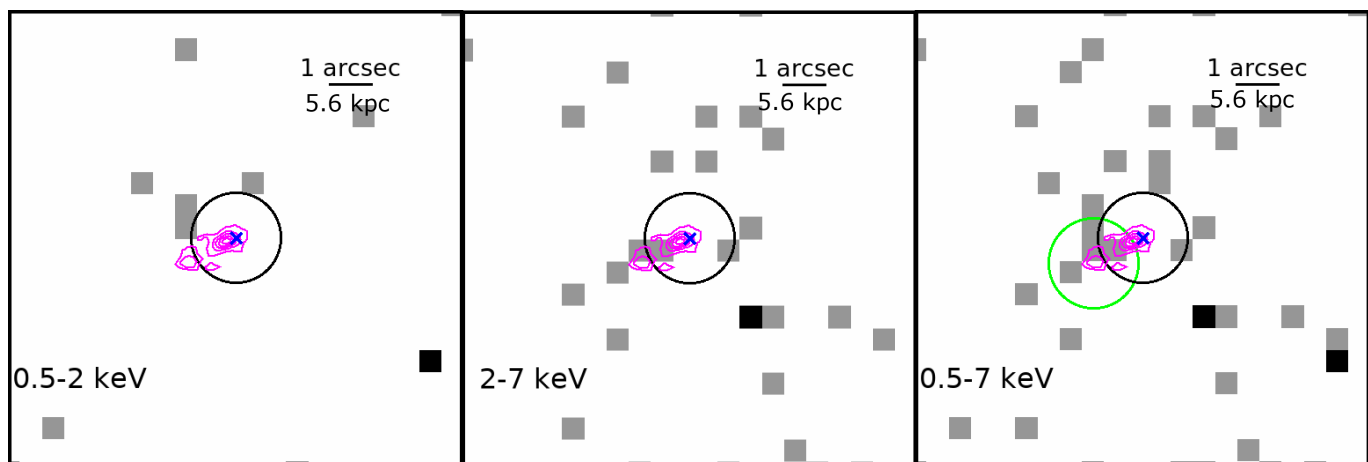


Fig. 1. *Chandra* $5'' \times 5''$ images in the soft, hard, and full bands for the total 177 ks exposure. North is up, East is left. The magenta contours show the [C II] emission detected with ALMA ($0.33'' \times 0.22''$ beam size) of the PSO167–13 (main emission) and companion (fainter emission to the south-east) system from 4σ to 20σ in steps of 4σ (Venemans et al. 2020, see also Neeleman et al. 2019). The blue X symbols mark the optical position of PSO167–13 (Venemans et al. 2020). The black circles denote the $1''$ extraction radius used throughout the text for PSO167–13. The green circle indicates the $1''$ extraction radius used for the companion galaxy (shown only in the right panel for clarity).

Table 1. Summary of the *Chandra* observations of PSO167–13. Data from OBSID 20397 were already presented in Vito et al. (2019a,b).

OBSID	Start date	T_{exp} [ks]
20397	2018-02-20	59.3
22523	2020-02-12	42.8
23153	2020-02-15	24.0
23018	2020-03-28	10.0
23199	2020-03-29	40.6

exposure. Then, we used the *wcs_match* and *wcs_update* tools to match the positions of the X-ray sources with > 10 counts to objects in the Pan-STARRS DR2 source mean catalog (Chambers et al. 2016)³ and correct the astrometry of the X-ray observations. The astrometry of the Pan-STARRS DR2 catalog is in turn registered to the Gaia DR2 astrometry (Gaia Collaboration et al. 2018). We could not directly use the Gaia catalog due to the small number of reliable counterparts of the X-ray sources. Finally, we merged the individual observations with the *reproject_obs* tool, and derived merged images and exposure maps. We repeated the detection procedure on the merged observation, and found a median difference between the position of the X-ray sources and the Pan-STARRS catalog of $\approx 0.3''$, which is consistent with the *Chandra* pixel size ($\approx 0.5''$). Only a few Gaia entries are associated unambiguously with X-ray sources, with offsets of ≈ 0.3 – $0.4''$, providing a useful consistency check.

We extracted response matrices and ancillary files from individual pointings using the *specextract* tool and added them using the *mathpha*, *addrmf*, and *addarf* HEASOFT tools⁴, weighting by the individual exposure times. Ancillary files, which are used to derive fluxes and luminosities, were aperture corrected.

2.2. Magellan/FIRE observations

We obtained near-infrared (NIR) spectroscopy for PSO167–13 in the range $\lambda = 0.8 - 2.5 \mu\text{m}$ with *Magellan*/FIRE during three

nights (March 3rd–5th 2020), for a total of 9.9 h on source. Observations were conducted during gray time, using the $1''$ wide slit in the high-resolution echellette mode, with a nominal resolution of $R=3600$. During these observations, the sky conditions were unstable, with rapidly varying seeing ($\approx 0.7'' - 2''$) and sky background. We rejected the exposures with seeing $> 1.5''$, lowering the useful amount of on-source time to 7.2 h on source. The individual spectra were obtained using the nodding technique ($3''$ nod length) in a sequence of ABBA acquisitions (44 exposures, each of 602.4 s). The data were reduced with the Interactive Data Language (IDL) pipeline FireHose v2 package (Gagné et al. 2015), and custom Python scripts. OH airglow was used to correct for telescope flexure and obtain the wavelength solution. Nearby A0V stars with airmass similar to that of the target were observed after each ABBA block in order to derive telluric absorption corrections and absolute flux calibrations, which we applied to the corresponding ABBA block, and define the extraction traces. We corrected for Galactic extinction ($E(B - V) = 0.0485$; from Schlafly & Finkbeiner (2011)) with the extinction curve of Fitzpatrick (1999).

3. Results

In this section, we report the results derived from the *Chandra* observations of PSO167–13 and the companion galaxy, and *Magellan*/FIRE spectroscopic observations of PSO167–13.

3.1. X-ray photometry of the companion galaxy

We present in Fig. 1 the *Chandra* images in the soft (0.5–2 keV), hard (2–7 keV), and full (0.5–7 keV) bands of the PSO167–13 system. As we did in Vito et al. (2019b), here we use a $1''$ radius extraction region (green circle in Fig. 1; corresponding to $\approx 90\%$ encircled energy fraction at 1.5 keV), centered on the ALMA position of the companion galaxy (RA=11:10:34.033, DEC=−13:29:46.29; Neeleman et al. 2019) to compute its photometry. We computed the detection significance in each energy band using the binomial no-source probability P_B presented by Weisskopf et al. (2007) and Broos et al. (2007), and set a signif-

³ <https://panstarrs.stsci.edu/>

⁴ <https://heasarc.gsfc.nasa.gov/docs/software/heasoft/>

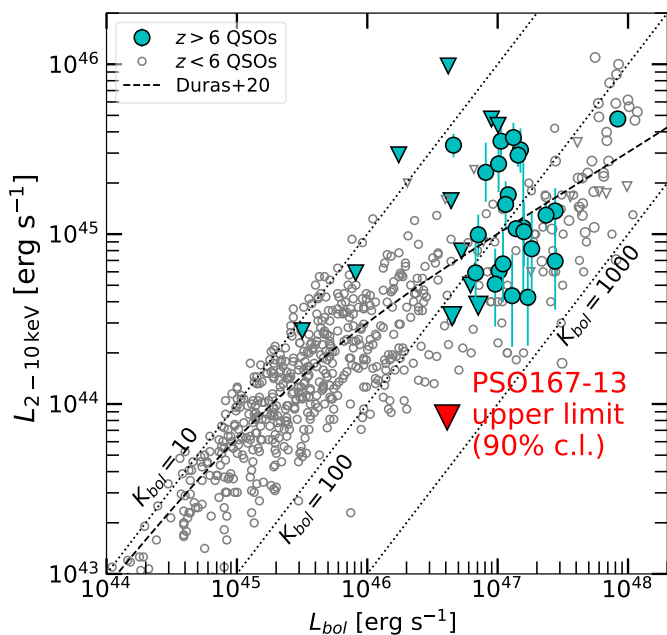


Fig. 2. X-ray luminosity versus bolometric luminosity for $z > 6$ QSOs (cyan symbols) from Connor et al. (2019, 2020), Vito et al. (2019a), Pons et al. (2020), and Wang et al. (2021a), compared with $z < 6$ QSOs (grey symbols) from Lusso et al. 2012; Martocchia et al. 2017; Nanni et al. 2017; Salvestrini et al. 2019, and the $L_X - L_{bol}$ relation (black dashed line) from Duras et al. (2020). Only radio-quiet QSOs are shown. Circles represent detected sources, and downward-pointing triangles mark upper limits. PSO167–13 is shown in red. Diagonal dotted lines mark the loci of constant bolometric correction (i.e., $K_{bol} = L_{bol}/L_X$).

icance threshold $(1 - P_B) = 0.99$ for source detection. We measured the X-ray background in an annular region with $R_{in} = 4''$ and $R_{out} = 24''$, where no bright X-ray sources are found. We detect 1, 3, and 4 counts in the soft, hard, and full bands. Considering the expected background of 0.35/0.59/0.93 counts, respectively, we obtained a detection significance $(1 - P_B) < 0.99$ (i.e., the galaxy is not detected) in all of the bands. Following the method of Weisskopf et al. (2007), we computed upper limits on the net counts $< 3.6, < 6.1,$ and < 7.1 in the soft, hard, and full bands, respectively.

In order to compute upper limits on the observed flux in the three bands, we assumed power-law emission with $\Gamma = 2$. This Γ value is typical of rapidly accreting SMBHs (Shemmer et al. 2008; Brightman et al. 2013, e.g.), and is consistent with the average photon index derived for optically selected QSOs up to $z \approx 7.5$ (e.g., Nanni et al. 2017; Bañados et al. 2018a; Vito et al. 2018b), although hints for steeper photon indexes at $z \gtrsim 6.5$ have been reported by Vito et al. (2019a) and Wang et al. (2021a). Accounting also for Galactic absorption toward the PSO167–13 system ($N_H = 4.7 \times 10^{20} \text{ cm}^{-2}$; e.g., Kalberla et al. 2005), we estimate fluxes $F < (1.9/6.6/5.0) \times 10^{-16} \text{ erg cm}^{-2} \text{ s}^{-1}$ in the soft/hard/full bands. Although the exact values of the upper limits depend on the choice of Γ , the errors on the flux are largely dominated by the statistical uncertainties on the X-ray counts. We computed the upper limit on the intrinsic 2–10 keV luminosity from the soft-band flux, consistently with previous works (e.g.; Vito et al. 2019b,a), as $L_X < 1.3 \times 10^{44} \text{ erg s}^{-1}$.

3.2. X-ray photometry of PSO167–13

We computed the X-ray photometry of PSO167–13 in a circular region of $R = 1''$ centered on the optical/NIR position of the QSO (RA=11:10:33.638, DEC=−13:29:45.73), which is provided by Venemans et al. (2020) based on the Gaia DR2 astrometry. They also report a small offset ($\approx 0.15''$) between the optical/NIR coordinates (blue cross in Fig. 1) and the peak position of the dust continuum and [C II] emission line of the QSO (magenta contours), possibly due to the QSO host galaxy being stretched during the ongoing interaction with the close companion galaxy (Venemans et al. 2020) and to the presence of a gas “bridge” component (Neeleman et al. 2019).

We detected 0, 2, and 2 counts in the soft, hard, and full bands, corresponding to $< 2.3, < 4.8,$ and < 4.5 net counts⁵, respectively (Weisskopf et al. 2007). As in § 3.1, we converted the upper limits on the counts into fluxes of $F < (1.2/5.1/3.2) \times 10^{-16} \text{ erg cm}^{-2} \text{ s}^{-1}$ in the soft/hard/full bands and a rest-frame 2–10 keV luminosity of $L_X < 8.3 \times 10^{43} \text{ erg s}^{-1}$. We note that one count in the hard band lies within the extraction regions of both the QSO and the companion galaxy, due to their small angular separation, such that the fluxes in the hard and full bands for at least one of these galaxies are overestimated. Fig. 2 presents the X-ray luminosity versus bolometric luminosity⁶ of QSOs at $z > 6$ and lower redshift. The upper limit on PSO167–13 at $L_{bol} = 4.1 \times 10^{46} \text{ erg s}^{-1}$ is significantly lower than the X-ray luminosity of X-ray detected QSOs at $z > 6$, and is a stronger constraint than the available upper limits on other undetected sources. The upper limit on L_X for PSO167–13 translates into a bolometric correction $K_{bol} = L_{bol}/L_X > 492$, to be compared with a typical value of $K_{bol} \approx 100$ for QSOs with similar bolometric luminosities.

The relative contribution of the X-ray and UV emission in QSOs is usually parametrized by the quantity $\alpha_{ox} = 0.38 \times \log(L_{2 \text{ keV}}/L_{2500 \text{ \AA}})$, which represents the slope of a nominal power-law connecting the emission in the two bands (e.g., Brandt & Alexander 2015 and references therein). We measure $L_{2500 \text{ \AA}} = 1.3 \times 10^{31} \text{ erg s}^{-1} \text{ Hz}^{-1}$ from the best-fitting UV continuum of the 2020 FIRE spectrum of PSO167–13 (see § 3.3) and convert the upper-limit on $L_{2-10 \text{ keV}}$ into $L_{2 \text{ keV}} < 1.07 \times 10^{26} \text{ erg s}^{-1} \text{ Hz}^{-1}$ (assuming power law emission with $\Gamma = 2$). From these values, we derived $\alpha_{ox} < -1.95$, which is the lowest value for a $z > 6$ QSO, and among the lowest values for the general QSO population (see Fig. 3).

A well-known anti-correlation exists between α_{ox} and L_{UV} up to $z > 6$ (e.g., Just et al. 2007; Lusso & Risaliti 2016; Martocchia et al. 2017; Nanni et al. 2017; Vito et al. 2019a). Therefore, a fairer comparison between QSOs with different UV luminosities can be made considering the values of $\Delta\alpha_{ox} = \alpha_{ox}^{obs} - \alpha_{ox}^{exp}$, i.e., the difference between the observed α_{ox} and the value expected for a given QSO’s UV luminosity. Assuming the Just et al. (2007) relation, as in Vito et al. (2019a), we find for PSO167–13 $\Delta\alpha_{ox} < -0.30$. The value of $\Delta\alpha_{ox}$ for PSO167–13 implies a factor of $\gtrsim 6$ weaker X-ray emission than the expectation, in agreement with the QSO location in Fig. 2. Among X-ray detected

⁵ The slightly lower upper limit on the net counts in the full band than that in the hard band is due to the higher background level.

⁶ Bolometric luminosities for $z > 6$ QSOs and for the Nanni et al. (2017) and Salvestrini et al. (2019) samples are estimated from $M_{1450 \text{ \AA}}$, using the bolometric correction of Venemans et al. (2016, see also Decarli et al. 2018), while values derived from SED fitting are plotted for the QSOs in the Lusso et al. (2012) and Martocchia et al. (2017) samples.

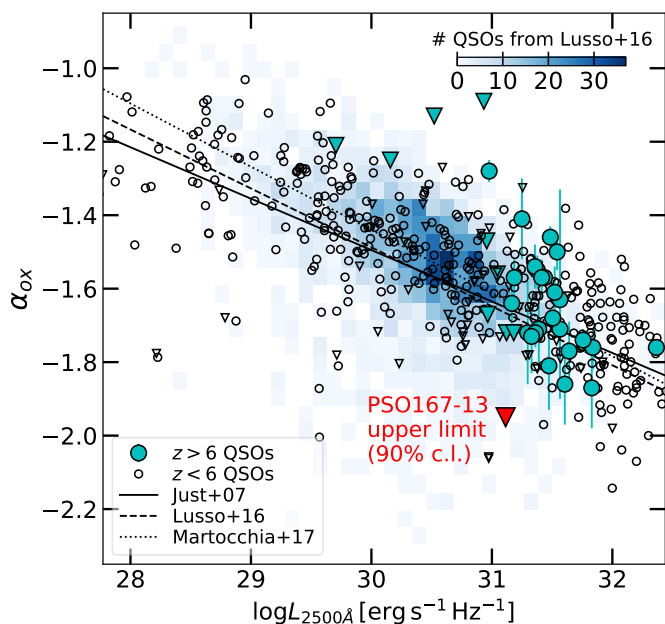


Fig. 3. α_{ox} plotted against UV luminosity for PSO167–13 (in red) and other $z > 6$ QSOs (cyan filled symbols) from Connor et al. (2019, 2020), Vito et al. (2019a), Wang et al. (2021a), and the updated values of the Pons et al. (2020) $z > 6.5$ QSOs (Pons et al. 2021). We also show $z < 6$ QSOs (black empty symbols and blue color map) from Shemmer et al. (2006); Steffen et al. (2006); Just et al. (2007); Lusso & Risaliti (2016); Nanni et al. (2017); Salvestrini et al. (2019), and best-fitting relations from Just et al. (2007), Lusso & Risaliti (2016), Martocchia et al. (2017). Circles represent detected sources, downward-pointing triangles mark upper limits. For visual purposes, we do not plot X-ray undetected sources included in the Lusso & Risaliti (2016) sample.

QSOs at $z > 6$, none shows such a level of X-ray weakness, and undetected sources have shallower upper limits (Fig. 4).

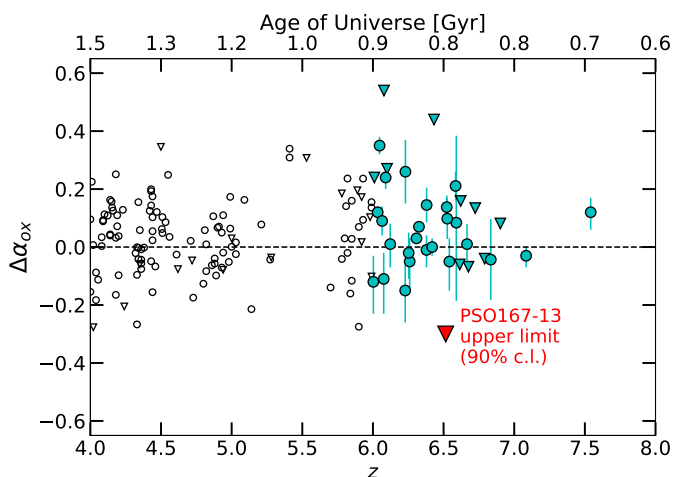


Fig. 4. $\Delta\alpha_{ox}$ as a function of redshift for $z > 4$ QSOs. Symbols are the same as in Fig. 3. The upper limit on PSO167–13 suggests it is the most extreme X-ray weak quasar yet known beyond $z > 4$.

3.3. Rest-frame UV spectroscopy of PSO167–13

Fig. 5 presents the rest-frame UV spectrum of PSO167–13 we obtained with *Magellan*/FIRE in 2020. We compare it with the 2014 spectrum presented by Venemans et al. (2015). After flux calibration, the normalization of the 2020 spectrum is $\approx 15\%$ lower than that reported in Venemans et al. (2015), most likely due to the varying seeing between the target and standard-star observations affecting the flux calibration in 2020. We therefore normalized the 2020 spectrum to the 2014 flux at 3000 \AA . Strong atmospheric absorption completely suppresses the QSO emission at rest-frame $\approx 1790 - 1900 \text{ \AA}$ and $\approx 2360 - 2690 \text{ \AA}$ (see the upper panel in Fig. 5). Therefore, we masked these two spectral windows in Fig. 5.

We fitted the rest-frame UV continuum to the unbinned 2020 spectrum in the spectral regions $2000-2350 \text{ \AA}$, $2690-2750 \text{ \AA}$, and $2850-3000 \text{ \AA}$ assuming a power-law of the form

$$F_{\lambda} = F_0 \left(\frac{\lambda}{2500 \text{ \AA}} \right)^{\alpha}. \quad (1)$$

The best-fitting slope $\alpha = -1.10 \pm 0.12$ is in agreement with the result of Mazzucchelli et al. (2017), and is redder than the typical QSO value ($\alpha = -1.7$; e.g., Selsing et al. 2016, see also Venemans et al. 2015).

3.3.1. Caveats on the rest-frame UV spectrum

Despite the longer on-source exposure, the 2020 *Magellan*/FIRE spectrum is noisier than the 2014 spectrum of PSO167–13, due to the poor atmospheric conditions reported in § 3.3. For instance, in the *H* band (where no strong QSO emission lines are expected at $z = 6.515$), we estimate a signal-to-noise ratio (SNR)⁷ of ≈ 3.0 and ≈ 4.5 for the 2020 and the 2014 spectra, respectively. In the following subsections, we describe the main spectral features visible in the spectrum, and the parameters derived with a basic analysis, for completeness. However, we warn that the results should be treated as merely indicative and with caution.

3.3.2. C IV emission line

Fig. 6 zooms into the $1.0 - 1.3 \mu\text{m}$ spectral region. The C IV (1549 \AA) emission line was not clearly detected in the 2014 spectrum (Mazzucchelli et al. 2017), but there is a tentative detection of this emission line in the 2020 spectrum, with a nominal total SNR ≈ 5 . Since it falls in a spectral region of relatively strong telluric absorption, it is unclear whether such a line is real or is partially or totally an artifact due to atmospheric correction. In this respect, future observations of PSO167–13 with *JWST* can confirm the presence and properties of this line.

Assuming this feature is real, we fitted the unbinned spectrum with a single Gaussian function to derive basic parameters using a χ^2 minimization approach. The line peaks at rest-frame $1525 \pm 4.4 \text{ \AA}$ (i.e., it is blueshifted by $\Delta v \approx -4565 \pm 859 \text{ km s}^{-1}$), with a $FWHM = 9063 \pm 2040 \text{ km s}^{-1}$ and rest-frame equivalent width (REW) of $32^{+15}_{-12} \text{ \AA}$. Absorption features might be present blueward of the Si IV and C IV emission lines, but a spectrum with higher SNR is required to test this scenario.

⁷ We used the DER_STEN algorithm of Stoehr et al. (2008), available at http://www.stecf.org/software/ASTROsoft/DER_SNR/

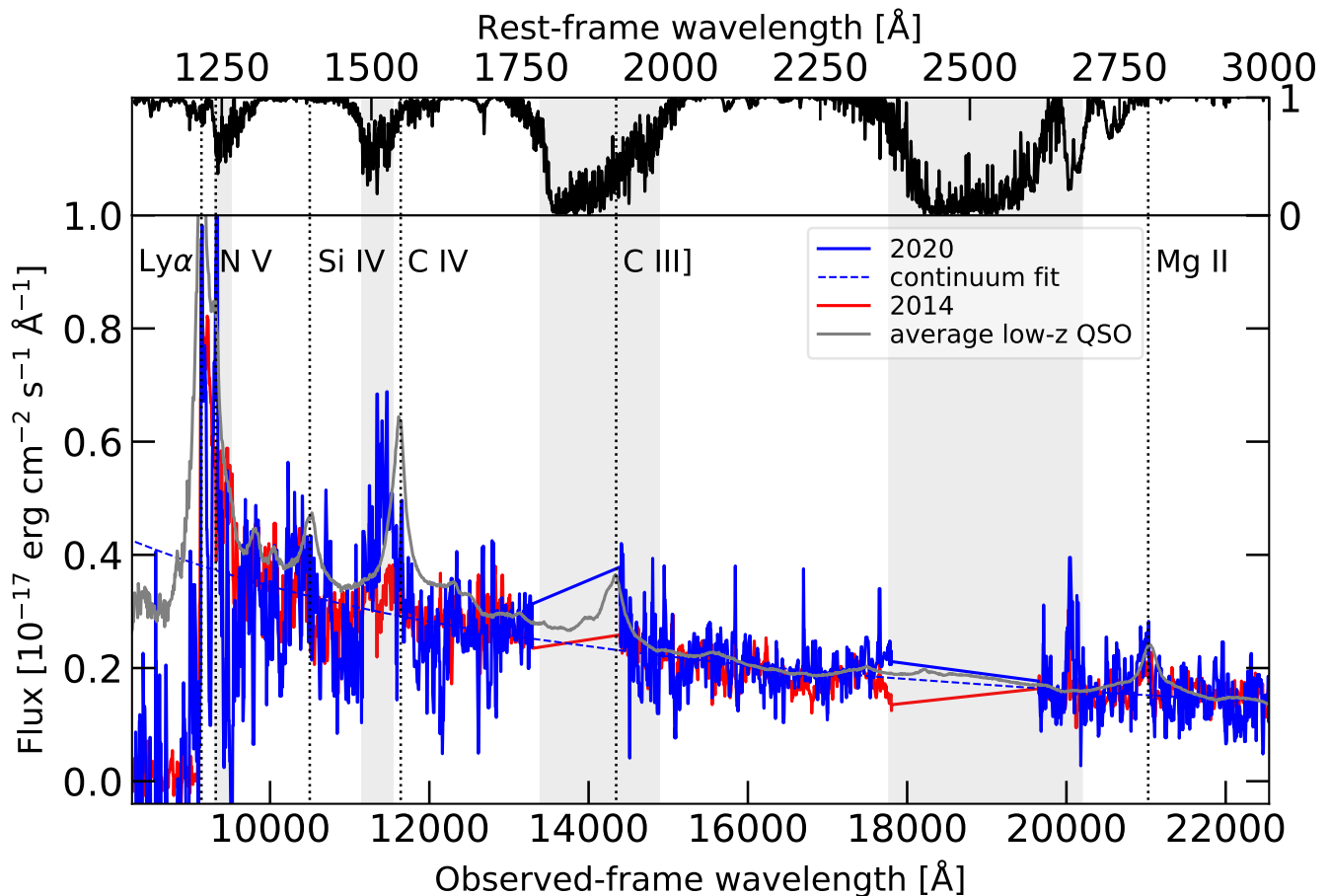


Fig. 5. *Bottom panel:* rest-frame UV spectrum of PSO167–13 obtained with our 2020 *Magellan*/FIRE observations (blue solid line), compared with the Venemans et al. (2015) spectrum (taken in 2014; red solid line). We applied a median filter with ≈ 20 Å kernel for visual purpose, as in Mazzucchelli et al. (2017). The average low-redshift QSO spectrum of Vanden Berk et al. (2001), normalized to the rest-frame 3000 Å flux of the Venemans et al. (2015) spectrum, is shown as a grey line. We also present the best-fitting UV power-law continuum of the 2020 spectrum as a dashed blue line, and the expected location of QSO emission lines at $z = 6.515$ as vertical dotted lines. *Top panel:* example of atmospheric transmission during our FIRE observations. Regions with transmission < 0.6 are marked with grey stripes in both panels. In particular, two spectral windows centered at rest-frame ≈ 1800 Å and ≈ 2500 Å are completely affected by the very low atmospheric transmission, and are thus masked in the spectra.

3.3.3. Mg II emission line

The Mg II (2798 Å) emission line is an important feature in the spectra of high-redshift QSOs, as it is often used to obtain single-epoch estimates of the SMBH mass (e.g., Vestergaard & Osmer 2009; Shen et al. 2011). Based on their analysis of the 2014 spectrum of PSO167–13, Mazzucchelli et al. (2017) reported a $\text{FWHM}_{\text{MgII}} = 2071^{+211}_{-354}$ km s $^{-1}$, and estimated $M_{\text{BH}} = 3 \times 10^8 M_{\odot}$ using the calibration of Vestergaard & Osmer (2009):

$$M_{\text{BH}} = 10^{6.86} \left(\frac{\text{FWHM}}{10^3 \text{ km s}^{-1}} \right)^2 \left(\frac{\lambda L_{\lambda 3000}}{10^{44} \text{ ergs}^{-1}} \right)^{0.5} M_{\odot} \quad (2)$$

Fig. 7 shows the PSO167–13 spectrum in the 2.0 – 2.2 μm spectral region. We fit the Mg II line assuming a QSO UV power-law continuum (Eq. 1), the Balmer pseudo-continuum modelled as in Schindler et al. (2020), the iron pseudo-continuum template of Vestergaard & Wilkes (2001), convolved with a Gaussian function with σ equal to that of the best-fitting Mg II line (see, e.g., Vestergaard & Wilkes 2001, Schindler et al. 2020), and

a single Gaussian function. The best-fitting model is shown as a dashed blue line in Fig. 7. The Gaussian is centered at rest-frame $\lambda = 2786 \pm 3$ Å; i.e., $\Delta v \approx -1268 \pm 306$ km s $^{-1}$ from the expected position given by the [C II] systemic redshift. The fit returns a $\text{REW}_{\text{MgII}} = 19^{+8}_{-6}$ Å, which is consistent with typical values for $z > 6$ QSOs (e.g., Onoue et al. 2020; Schindler et al. 2020).

The Mg II width ($\text{FWHM}_{\text{MgII}} = 3947 \pm 758$ km s $^{-1}$) is significantly larger than the value found by Mazzucchelli et al. (2017), and translates into $M_{\text{BH}} = 1.1 \times 10^9 M_{\odot}$ ⁸ and an Eddington ratio $\lambda_{\text{Edd}} = 0.3$. We caution that the line’s blueshift may indicate the presence of outflowing nuclear winds (see § 4.3), in which case the virial assumption upon which the BH mass estimate is based would be affected. In addition, the limited spectral quality and the different BH mass value obtained from the 2014 spectrum lead us to refrain from over-interpreting these results.

⁸ Errors on single-epoch black-hole mass estimates are dominated by systematic uncertainties of the calibration (> 0.5 dex; e.g., Shen 2013 and references therein).

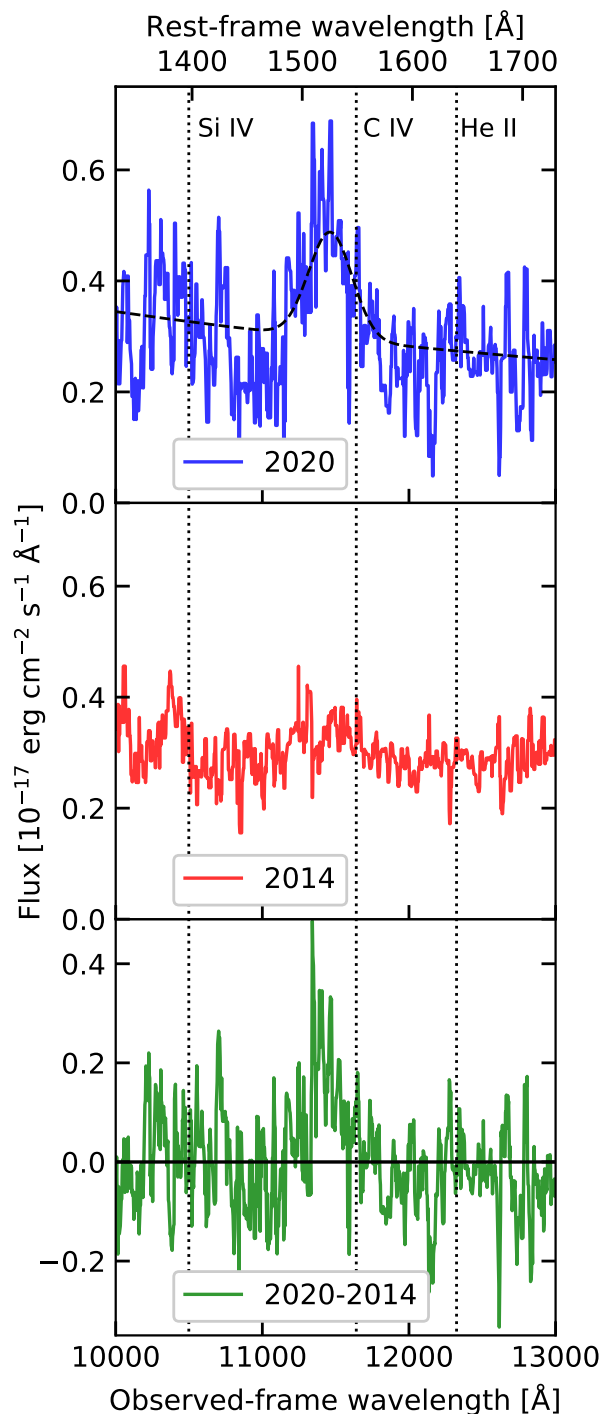


Fig. 6. Zoom of the spectral region of the 2020 (top panel) and 2014 (middle panel) spectra encompassing the C IV emission line of PSO167–13. The bottom panel presents the difference of the two epochs. The dashed black line in the top panel marks the best-fitting continuum plus single Gaussian model of the C IV emission line.

4. Discussion

4.1. X-ray emission from the companion galaxy

In Vito et al. (2019b), we discussed the detection of a faint and hard X-ray source in the PSO167–13 system, consistent with

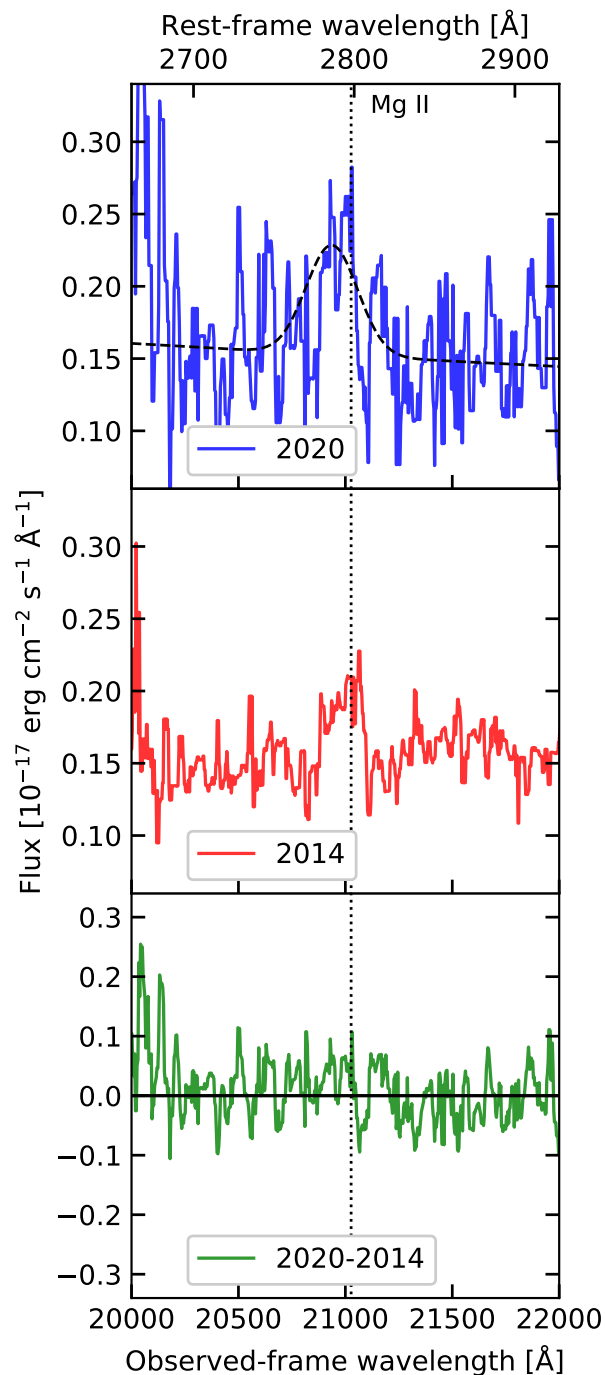


Fig. 7. Zoom of the spectral region of the 2020 (top panel) and 2014 (middle panel) spectra encompassing the Mg II emission line of PSO167–13. The bottom panel presents the difference of the two epochs. The dashed black line in the top panel marks the best-fitting continuum plus single Gaussian model of the Mg II emission line.

the position of the companion galaxy, although the relatively large positional uncertainty prevented us from discarding an association with the optical QSO. If the X-ray source had been confirmed with the new *Chandra* observations and an unambiguous association with the companion galaxy had been obtained, it would have been considered a (obscured) QSO, and

the PSO167–13 system would have been a QSO pair at high redshift.

Considering the total 177 ks coverage (§ 3.1), the significance of the emission in the full band ($P = 0.985$) is slightly below the detection threshold used in Vito et al. (2019b,a, i.e.; $P = 0.99$), and is dominated by the three counts that were already reported in Vito et al. (2019b). We note that in that work we used a narrower energy band for detection (i.e., 2–5 keV). Repeating the detection procedure in that band including the new *Chandra* observations, the emission is still nominally significant ($P = 0.992$), with $2.6^{+2.1}_{-1.4}$ net counts, implying $F_{2-5\text{keV}} = 1.38^{+1.11}_{-0.74} \times 10^{-16} \text{ erg cm}^{-2} \text{ s}^{-1}$.

Based on the three net counts detected in 59.3 ks in the 2018 pointing (Vito et al. 2019b), we would have expected to detect 5.7 counts in the new observations (117.4 ks), if the detection were real (i.e. not due to spurious background emission) and not highly variable. Instead, we detected none, corresponding to a Poisson probability $P(k = 0, \mu = 5.7) = 0.003$. Therefore, either the counts detected in the 2018 observation were due to a strong background fluctuation (in Vito et al. 2019b we assigned a probability of 4×10^{-4} to this possibility), or the X-ray source is variable at 0.997 significance. In the latter case, comparing the flux derived in Vito et al. (2019b, i.e., $F_{2-5\text{keV}} = 8^{+6}_{-4} \times 10^{-16} \text{ erg cm}^{-2} \text{ s}^{-1}$) with the flux computed from the new 117.4 ks only (i.e., $F_{2-5\text{keV}} < 2 \times 10^{-16} \text{ erg cm}^{-2} \text{ s}^{-1}$), the X-ray source would have dimmed by a factor of ≈ 4 from 2018 to 2020; i.e., about three months in the QSO rest frame. A similar variability (i.e., a factor of ≈ 2.5 in flux over a period of ≈ 2 years in the rest frame) was reported by Nanni et al. (2017) for another $z > 6$ QSO, namely SDSS J1030+0524 (see also Shemmer et al. 2005 for a $z = 5.41$ SDSS QSO).

Whatever the cause, we do not confirm the presence of significant X-ray emission from the PSO167–13 system, and in particular from the companion galaxy. To date, out of the ≈ 20 companion galaxies currently detected with *ALMA* close to $z > 6$ QSOs (Willott et al. 2017; Decarli et al. 2017, 2018; Neeleman et al. 2019; Venemans et al. 2020), none has been detected in the X-rays with high significance (i.e., $P > 0.99$; see also Connor et al. 2019, 2020).

4.2. X-ray weakness of PSO167–13

The X-ray weakness of PSO167–13 discussed in § 3.2, i.e., > 6 weaker than expected based on its UV luminosity, is notable. BAL QSOs have been generally found to be X-ray weak, by factors up to ≈ 100 in extreme cases (e.g., Gallagher et al. 2006; Gibson et al. 2009; Luo et al. 2014; Liu et al. 2018), which is possibly linked to the acceleration of nuclear winds in these objects (see § 4.3).

Among the general SDSS radio-quiet and non-BAL QSO population, Pu et al. (2020) found that only $\approx 6\%$ show similar levels of X-ray weakness, and they are preferentially WLQs or red QSOs (see also, e.g., Ni et al. 2018; Timlin et al. 2020b). Applying this fraction to the total number of $z > 6$ QSOs currently observed in the X-ray band (i.e., 36; Vito et al. 2019a and references therein, Connor et al. 2019, 2020; Pons et al. 2020; Wang et al. 2021a) we expect ≈ 2 of them to be X-ray weak by factors greater than six. However, we note that some $z > 6$ QSOs with X-ray observations are BAL QSOs (e.g., Fan et al. 2003; Matsuoka et al. 2016; Connor et al. 2020). Hence, they should not be considered here for a proper comparison with the Pu et al. (2020) sample, which includes only radio-quiet and non-BAL QSOs, thus decreasing the expected number of X-ray weak QSOs at

$z > 6$. Given the quality of the currently available rest-frame spectrum, PSO167–13 cannot be securely identified either as a WLQ or BAL QSO, although there might be evidence for the presence of nuclear winds (see § 4.3).

Several physical reasons can be invoked to explain the lack of strong X-ray emission from a type 1 QSO:

1. Intrinsic X-ray weakness may be caused by a different geometry or physics of the hot corona from those of typical QSOs. For instance, the hot corona may be quenched, disrupted, or not yet formed, due to currently not well understood causes (e.g., Leighly et al. 2007, Luo et al. 2013, Luo et al. 2014, Liu et al. 2018). In this case, the accretion disk can remain largely unaffected, and emit UV photons as a typical QSO.
2. Absorption on scales smaller than most of the accretion disk (e.g., due to a thick inner disk, a “failed wind”, or the outflowing material itself in the case of radiation-pressure confinement; e.g., Proga & Kallman 2004; Baskin et al. 2014; Ni et al. 2018; Liu et al. 2021) can absorb the X-ray photons from the hot corona, leaving the UV emission from the accretion disk largely unaffected, thus resulting in significant X-ray weakness observed for type 1 QSOs.
3. Intrinsic variability can cause a QSO to be observed during periods of low X-ray flux state (e.g., Pu et al. 2020, and references therein), although luminous QSOs often do not show large variability amplitudes (e.g., Paolillo et al. 2017; Shemmer et al. 2017). For instance, Timlin et al. (2020a) found that QSOs with UV luminosity similar to that of PSO167–13 vary by a factor of < 3 .
4. Occultation events of broad emission-line clouds with angular size comparable to that of the hot corona can obscure the X-ray emission, although they are usually found to happen on shorter rest-frame timescales (a few hours) than those we probe for PSO167–13 (e.g., Risaliti et al. 2011; De Marco et al. 2020).

Assuming that the X-ray emission of PSO167–13 is absorbed by intervening neutral material with solar metallicity, and that the intrinsic X-ray luminosity is consistent with the $\alpha_{\text{ox}} - L_{\text{UV}}$ relation (i.e., $L_{2-10\text{keV}} = 5.1 \times 10^{44} \text{ erg s}^{-1}$), we used the self-consistent MYTorus model (Murphy & Yaqoob 2009) in XSPEC to estimate the equivalent hydrogen column density required to match the upper limits on flux reported in § 3.2. We fixed the intrinsic powerlaw slope to $\Gamma = 2$, the normalization of the scattered and line components to that of the transmitted component, and the inclination angle to 90 deg. We found that absorption due to Compton-thick ($N_{\text{H}} \gtrsim 10^{24} \text{ cm}^{-2}$) material is required. However, the physical and geometrical assumptions of the MYTorus model might not be a good representation of the obscuring material in the inner regions on PSO167–13, which is expected to lie on smaller scales than the accretion disk to allow for the detection of the UV emission. Using a simple absorbed powerlaw model in XSPEC (model *zwabs* \times *powerlaw*), which however does not include a treatment of photon scattering, the column densities required to match the observed fluxes in the soft and hard bands are $N_{\text{H}} \gtrsim 2 \times 10^{24} \text{ cm}^{-2}$ and $N_{\text{H}} \gtrsim 9 \times 10^{24} \text{ cm}^{-2}$, respectively. Constraining such high values of N_{H} is possible thanks to the high-redshift nature of this QSO, which shifts the photoelectric cut-off to low observed energies even for large column densities,⁹ its relatively high UV luminosity (and, hence, expected X-ray luminosity), and the depth of the

⁹ The *Chandra* bandpass samples the rest-frame energy range 4–50 keV at $z = 6.515$.

available *Chandra* observations. We conclude that the most plausible causes of the lack of strong X-ray emission from PSO167–13 are either intrinsic X-ray weakness, possibly due to an accretion mechanism different from that of typical QSOs, or small-scale absorption by Compton thick material.

4.3. Possible nuclear winds in PSO167–13

Both the C IV and Mg II emission lines in the UV spectrum of PSO167–13 show large tentative blueshifts with respect to the [C II] systemic redshift ($-4565 \pm 859 \text{ km s}^{-1}$ and $-1268 \pm 306 \text{ km s}^{-1}$, respectively), although the derivation of accurate physical parameters for these lines is affected by the low SNR of the spectrum, and, in particular for the C IV line, by the low atmospheric transmission. We also note that absorption features blueward of the C IV line may be present, similar to the blueshifted features in BAL QSOs. Rapidly accreting QSOs, WLQs (which are thought to be accreting close to the Eddington limit), and, in particular, high-redshift QSOs often exhibit similarly large or even larger C IV and Mg II blueshifts (e.g., Luo et al. 2015; Plotkin et al. 2015; Vietri et al. 2018, 2020; Venemans et al. 2016; Ni et al. 2018; Yi et al. 2019; Onoue et al. 2020; Schindler et al. 2020, Yi et al. in prep), which are usually considered to be produced by outflowing winds.

In this respect, the X-ray weakness of PSO167–13 (either intrinsic or due to small-scale obscuration) may play an important role in the acceleration mechanisms of such winds. In fact, X-ray weakness can help avoid the overionization of the accreting gas, thus allowing efficient launching of UV-line driven winds (e.g., Proga et al. 2000; Proga & Kallman 2004; Baskin et al. 2014). Therefore, it is perhaps not surprising that a relation has been found between α_{ox} and the blueshift of the C IV emission line (e.g., Richards et al. 2011; Timlin et al. 2020b; Vietri et al. 2020), in the sense that objects with larger C IV blueshifts have softer (i.e., UV dominated) spectra. For instance, the values of α_{ox} and C IV blueshift of PSO167–13 are consistent with the relations found by Timlin et al. (2020b) and Zappacosta et al. (2020), although for QSOs with ≈ 1 dex higher bolometric luminosities.

While the C IV emission line in QSOs is usually found to be blueshifted by $\approx 1000 \text{ km s}^{-1}$ with respect to the Mg II line (e.g., Meyer et al. 2019), evidence has been found recently for an increasing $\Delta v(\text{CIV} - \text{MgII})$ at $z > 6$ (Meyer et al. 2019; Schindler et al. 2020, but see also Shen et al. 2019), with an average value of $\approx -3000 \text{ km s}^{-1}$ and up to $\approx -5000 \text{ km s}^{-1}$ at $z = 6.5$. For PSO167–13, we found $\Delta v(\text{CIV} - \text{MgII}) = -3300 \text{ km s}^{-1}$, in agreement with the results of Schindler et al. (2020) at similar redshift, but for QSOs which are typically ≈ 1 dex more luminous in the UV. A higher signal-to-noise NIR spectrum is required to confirm the tentative nature of the rest-frame UV line properties of this PSO167–13.

5. Conclusions

We present deep X-ray (*Chandra*, 177 ks in total) and NIR spectroscopic (*Magellan*/FIRE, 7.2h on source) follow-up observations of PSO167–13, an optically selected $z = 6.515$ QSO ($M_{1450 \text{ \AA}} = -25.6$) in an interacting system with a close ($0.9''$, corresponding to ≈ 5 projected kpc) companion galaxy detected with both ALMA and HST. A previous tentative detection of a hard X-ray source with *Chandra* (59.3 ks) suggested the presence of obscured nuclear accretion in this system. We summarize here the main results:

- The new *Chandra* observations do not confirm significant X-ray emission from the QSO-galaxy system, suggesting that the previously detected X-ray source was due to a strong background fluctuation, although intrinsic variability by a factor ≈ 4 cannot be excluded.
- We calculate upper limits (at the 90% confidence level) on the X-ray flux of the companion galaxy ($F < (1.9/6.6/5.0) \times 10^{-16} \text{ erg cm}^{-2} \text{ s}^{-1}$ in the soft/hard/full bands) and the intrinsic 2–10 keV luminosity ($L_X < 1.3 \times 10^{44} \text{ erg s}^{-1}$). To date, none of the ALMA detected companion galaxies in the proximity of $z > 6$ QSOs has been detected with high significance ($P > 0.99$) in standard X-ray bands.
- Likewise, we place upper limits on the X-ray flux from PSO167–13 of $F < (1.2/5.1/3.2) \times 10^{-16} \text{ erg cm}^{-2} \text{ s}^{-1}$ in the soft/hard/full bands and intrinsic luminosity $L_{2-10 \text{ keV}} < 8.3 \times 10^{43} \text{ erg s}^{-1}$. These are the lowest upper limits on the X-ray emission for a $z > 6$ QSO.
- The ratio between the X-ray and UV luminosity of PSO167–13, $\alpha_{\text{ox}} < -1.95$, makes PSO167–13 an outlier from the $\alpha_{\text{ox}} - L_{\text{UV}}$ relation for QSOs, with a deviation of $\Delta\alpha_{\text{ox}} < -0.30$, corresponding to a factor > 6 weaker X-ray emission than the expectation. Only $\approx 6\%$ of SDSS radio-quiet non-BAL QSOs show similar X-ray weakness, and they are usually WLQs or red QSOs. Such weak X-ray emission for PSO167–13 could be intrinsic (e.g., due to an accretion configuration different from typical optically selected QSOs), or due to small-scale obscuration, which would allow the detection of the UV continuum. In the latter case, we estimate a column density of $N_H > 10^{24} \text{ cm}^{-2}$.
- The slope of the rest-frame UV spectrum of PSO167–13 taken in 2020 and presented here ($\alpha = -1.10 \pm 0.12$) is consistent with previous spectroscopy, and redder than typical values for optically selected QSOs. Absorption features may be present blueward of the C IV line, but the low SNR of the spectrum prevents their definitive assessment.
- The tentatively detected C IV and Mg II emission lines appear to be broad ($FWHM = 9063 \pm 2040 \text{ km s}^{-1}$ and $3947 \pm 758 \text{ km s}^{-1}$, respectively) and strongly blueshifted from the systemic redshift based on the [C II] $158\mu\text{m}$ line ($\Delta v = -4565 \text{ km s}^{-1}$ and -1268 km s^{-1} , respectively). Similar large blueshifts have been found in other $z > 6$ QSOs, and in rapidly accreting QSOs and WLQs at lower redshifts, and are generally associated with the presence of nuclear winds. The C IV line is found to be blueshifted with respect to the Mg II line by $\Delta v(\text{CIV} - \text{MgII}) = -3300 \text{ km s}^{-1}$. This value is consistent with recent findings for $z > 6$ QSOs. However, we note that the spectroscopic observations were taken during nights with poor seeing and strongly varying atmospheric conditions. A higher signal-to-noise NIR spectrum is required to confirm the tentative nature of the rest-frame UV line properties of this PSO167–13.
- As suggested by the relation between α_{ox} and C IV blueshift found by previous works, the unusual X-ray weakness of PSO167–13 might facilitate the acceleration of such winds by preventing the overionization of the accreting material, which is required by models of UV-driven wind acceleration. Based on the $FWHM$ of the Mg II line, we estimate a virial BH mass of $1.1 \times 10^9 M_\odot$, corresponding to $\lambda_{\text{Edd}} = 0.3$, but we caution that the presence of nuclear winds could severely affect this measurement.

Acknowledgements. We thank the referee, Belinda Wilkes, for her useful comments and suggestions. We thank Marcel Neeleman, Bram Venemans, Estelle Pons, and Weimin Yi for useful discussions, and Marianne Vestergaard for providing the iron UV emission template of Vestergaard & Wilkes (2001). We acknowledge support from CXC grants GO0-21078D (W.N.B.) and GO0-21078C

(O.S.), from ANID grants CATA-Basal AFB-170002 (F.E.B., E.C.), FONDECYT Regular 1190818 (F.E.B.) and 1200495 (F.E.B.), Millennium Science Initiative ICN12_009 (F.E.B.), the NSFC grant 11991053 and National Key R&D Program of China grant 2016YFA0400702 (B.L.), from ASI-INAF n. 2018-31-HH.0 grant and PRIN-MIUR 2017 (S.G.), and from the agreement ASI-INAF n. 2017-14-H.O. The work of T.C. was carried out at the Jet Propulsion Laboratory, California Institute of Technology, under a contract with NASA. This research has made use of data obtained from the Chandra Data Archive (Proposal IDs 19700183 and 21700027), and software provided by the Chandra X-ray Center (CXC) in the application packages CIAO. This paper includes data gathered with the 6.5 meter Magellan Telescopes located at Las Campanas Observatory, Chile (CNTAC proposal ID CN2020A-22). This research made use of SAO Image DS9 Joye & Mandel (2003) and Astropy,¹⁰ a community-developed core Python package for Astronomy (Astropy Collaboration et al. 2013, 2018).

References

- Astropy Collaboration, Price-Whelan, A. M., Sipőcz, B. M., et al. 2018, *AJ*, 156, 123
- Astropy Collaboration, Robitaille, T. P., Tollerud, E. J., et al. 2013, *A&A*, 558, A33
- Bañados, E., Connor, T., Stern, D., et al. 2018a, *ApJ*, 856, L25
- Bañados, E., Venemans, B. P., Decarli, R., et al. 2016, *ApJS*, 227, 11
- Bañados, E., Venemans, B. P., Mazzucchelli, C., et al. 2018b, *Nature*, 553, 473
- Baskin, A., Laor, A., & Stern, J. 2014, *MNRAS*, 445, 3025
- Belladitta, S., Moretti, A., Caccianiga, A., et al. 2020, *A&A*, 635, L7
- Brandt, W. N. & Alexander, D. M. 2015, *A&A Rev.*, 23, 1
- Brightman, M., Silverman, J. D., Mainieri, V., et al. 2013, *MNRAS*, 433, 2485
- Broos, P. S., Feigelson, E. D., Townsley, L. K., et al. 2007, *ApJS*, 169, 353
- Chambers, K. C., Magnier, E. A., Metcalfe, N., et al. 2016, *arXiv e-prints*, arXiv:1612.05560
- Connor, T., Bañados, E., Mazzucchelli, C., et al. 2020, *ApJ*, 900, 189
- Connor, T., Bañados, E., Stern, D., et al. 2019, *ApJ*, 887, 171
- Davies, F. B., Hennawi, J. F., & Eilers, A.-C. 2019, *ApJ*, 884, L19
- De Marco, B., Adhikari, T. P., Pontì, G., et al. 2020, *A&A*, 634, A65
- De Rosa, G., Venemans, B. P., Decarli, R., et al. 2014, *ApJ*, 790, 145
- Decarli, R., Dotti, M., Bañados, E., et al. 2019, *ApJ*, 880, 157
- Decarli, R., Walter, F., Venemans, B. P., et al. 2017, *Nature*, 545, 457
- Decarli, R., Walter, F., Venemans, B. P., et al. 2018, *ApJ*, 854, 97
- Duras, F., Bongiorno, A., Ricci, F., et al. 2020, *A&A*, 636, A73
- Eilers, A.-C., Hennawi, J. F., & Davies, F. B. 2018, *ApJ*, 867, 30
- Eilers, A.-C., Hennawi, J. F., Decarli, R., et al. 2020, *ApJ*, 900, 37
- Fan, X., Strauss, M. A., Schneider, D. P., et al. 2003, *AJ*, 125, 1649
- Fan, X., Wang, F., Yang, J., et al. 2019, *ApJ*, 870, L11
- Farina, E. P., Arrigoni-Battaia, F., Costa, T., et al. 2019, *ApJ*, 887, 196
- Fitzpatrick, E. L. 1999, *PASP*, 111, 63
- Fruscione, A., McDowell, J. C., Allen, G. E., et al. 2006, *Society of Photo-Optical Instrumentation Engineers (SPIE) Conference Series*, Vol. 6270, CIAO: Chandra's data analysis system, 62701V
- Gagné, J., Lambrides, E., Faherty, J. K., & Simcoe, R. 2015, *Firehose_V2: Firehose V2.0*
- Gaia Collaboration, Brown, A. G. A., Vallenari, A., et al. 2018, *A&A*, 616, A1
- Gallagher, S. C., Brandt, W. N., Chartas, G., et al. 2006, *ApJ*, 644, 709
- Gallerani, S., Zappacosta, L., Orofino, M. C., et al. 2017, *MNRAS*, 467, 3590
- Gibson, R. R., Jiang, L., Brandt, W. N., et al. 2009, *ApJ*, 692, 758
- Jiang, L., McGreer, I. D., Fan, X., et al. 2016, *ApJ*, 833, 222
- Joye, W. A. & Mandel, E. 2003, in *Astronomical Society of the Pacific Conference Series*, Vol. 295, *Astronomical Data Analysis Software and Systems XII*, ed. H. E. Payne, R. I. Jedrzejewski, & R. N. Hook, 489
- Just, D. W., Brandt, W. N., Shemmer, O., et al. 2007, *ApJ*, 665, 1004
- Kalberla, P. M. W., Burton, W. B., Hartmann, D., et al. 2005, *A&A*, 440, 775
- Leighly, K. M., Halpern, J. P., Jenkins, E. B., et al. 2007, *ApJ*, 663, 103
- Liu, H., Luo, B., Brandt, W. N., et al. 2021, *arXiv e-prints*, arXiv:2102.02832
- Liu, H., Luo, B., Brandt, W. N., Gallagher, S. C., & Garmire, G. P. 2018, *ApJ*, 859, 113
- Luo, B., Brandt, W. N., Alexander, D. M., et al. 2013, *ApJ*, 772, 153
- Luo, B., Brandt, W. N., Alexander, D. M., et al. 2014, *ApJ*, 794, 70
- Luo, B., Brandt, W. N., Hall, P. B., et al. 2015, *ApJ*, 805, 122
- Lusso, E., Comastri, A., Simmons, B. D., et al. 2012, *MNRAS*, 425, 623
- Lusso, E. & Risaliti, G. 2016, *ApJ*, 819, 154
- Martocchia, S., Piconcelli, E., Zappacosta, L., et al. 2017, *A&A*, 608, A51
- Matsuoka, Y., Onoue, M., Kashikawa, N., et al. 2018a, *PASJ*, 70, S35
- Matsuoka, Y., Onoue, M., Kashikawa, N., et al. 2016, *ApJ*, 828, 26
- Matsuoka, Y., Onoue, M., Kashikawa, N., et al. 2019, *ApJ*, 872, L2
- Matsuoka, Y., Strauss, M. A., Kashikawa, N., et al. 2018b, *ApJ*, 869, 150
- Mazzucchelli, C., Bañados, E., Venemans, B. P., et al. 2017, *ApJ*, 849, 91
- Mazzucchelli, C., Decarli, R., Farina, E. P., et al. 2019, *ApJ*, 881, 163
- Meyer, R. A., Bosman, S. E. I., & Ellis, R. S. 2019, *MNRAS*, 487, 3305
- Mignoli, M., Gilli, R., Decarli, R., et al. 2020, *A&A*, 642, L1
- Murphy, K. D. & Yaqoob, T. 2009, *MNRAS*, 397, 1549
- Nanni, R., Gilli, R., Vignali, C., et al. 2018, *A&A*, 614, A121
- Nanni, R., Vignali, C., Gilli, R., Moretti, A., & Brandt, W. N. 2017, *A&A*, 603, A128
- Neeleman, M., Bañados, E., Walter, F., et al. 2019, *ApJ*, 882, 10
- Ni, Q., Brandt, W. N., Luo, B., et al. 2018, *MNRAS*, 480, 5184
- Onoue, M., Bañados, E., Mazzucchelli, C., et al. 2020, *ApJ*, 898, 105
- Onoue, M., Kashikawa, N., Matsuoka, Y., et al. 2019, *ApJ*, 880, 77
- Pacucci, F., Ferrara, A., Volonteri, M., & Dubus, G. 2015, *MNRAS*, 454, 3771
- Paolillo, M., Papadakis, I., Brandt, W. N., et al. 2017, *MNRAS*, 471, 4398
- Planck Collaboration, Ade, P. A. R., Aghanim, N., et al. 2016, *A&A*, 594
- Plotkin, R. M., Shemmer, O., Trakhtenbrot, B., et al. 2015, *ApJ*, 805, 123
- Pons, E., McMahon, R. G., Banerji, M., & Reed, S. L. 2020, *MNRAS*, 491, 3884
- Pons, E., McMahon, R. G., Banerji, M., & Reed, S. L. 2021, *MNRAS*, 501, 6208
- Proga, D. & Kallman, T. R. 2004, *ApJ*, 616, 688
- Proga, D., Stone, J. M., & Kallman, T. R. 2000, *ApJ*, 543, 686
- Pu, X., Luo, B., Brandt, W. N., et al. 2020, *ApJ*, 900, 141
- Reed, S. L., Banerji, M., Becker, G. D., et al. 2019, *MNRAS*, 487, 1874
- Richards, G. T., Kruczek, N. E., Gallagher, S. C., et al. 2011, *AJ*, 141, 167
- Risaliti, G., Nardini, E., Salvati, M., et al. 2011, *MNRAS*, 410, 1027
- Salvestrini, F., Risaliti, G., Bisogni, S., Lusso, E., & Vignali, C. 2019, *A&A*, 631, A120
- Schindler, J.-T., Farina, E. P., Bañados, E., et al. 2020, *ApJ*, 905, 51
- Schlafly, E. F. & Finkbeiner, D. P. 2011, *ApJ*, 737, 103
- Selsing, J., Fynbo, J. P. U., Christensen, L., & Krogager, J. K. 2016, *A&A*, 585, A87
- Shemmer, O., Brandt, W. N., Netzer, H., Maiolino, R., & Kaspi, S. 2006, *ApJ*, 646, L29
- Shemmer, O., Brandt, W. N., Netzer, H., Maiolino, R., & Kaspi, S. 2008, *ApJ*, 682, 81
- Shemmer, O., Brandt, W. N., Paolillo, M., et al. 2017, *ApJ*, 848, 46
- Shemmer, O., Brandt, W. N., Vignali, C., et al. 2005, *ApJ*, 630, 729
- Shen, Y. 2013, *Bulletin of the Astronomical Society of India*, 41, 61
- Shen, Y., Richards, G. T., Strauss, M. A., et al. 2011, *ApJS*, 194, 45
- Shen, Y., Wu, J., Jiang, L., et al. 2019, *ApJ*, 873, 35
- Simcoe, R. A., Burgasser, A. J., Bernstein, R. A., et al. 2008, in *Society of Photo-Optical Instrumentation Engineers (SPIE) Conference Series*, Vol. 7014, *Ground-based and Airborne Instrumentation for Astronomy II*, ed. I. S. McLean & M. M. Casali, 70140U
- Spingola, C., Dallacasa, D., Belladitta, S., et al. 2020, *A&A*, 643, L12
- Steffen, A. T., Strateva, I., Brandt, W. N., et al. 2006, *AJ*, 131, 2826
- Stoehr, F., White, R., Smith, M., et al. 2008, in *Astronomical Society of the Pacific Conference Series*, Vol. 394, *Astronomical Data Analysis Software and Systems XVII*, ed. R. W. Argyle, P. S. Bunclark, & J. R. Lewis, 505
- Timlin, John D., I., Brandt, W. N., Zhu, S., et al. 2020a, *MNRAS*, 498, 4033
- Timlin, J. D., Brandt, W. N., Ni, Q., et al. 2020b, *MNRAS*, 492, 719
- Valiante, R., Agarwal, B., Habouzit, M., & Pezzulli, E. 2017, *Publications of the Astronomical Society of Australia*, 34, e031
- Vanden Berk, D. E., Richards, G. T., Bauer, A., et al. 2001, *AJ*, 122, 549
- Venemans, B. P., Bañados, E., Decarli, R., et al. 2015, *ApJ*, 801, L11
- Venemans, B. P., Walter, F., Neeleman, M., et al. 2020, *ApJ*, 904, 130
- Venemans, B. P., Walter, F., Zschaechner, L., et al. 2016, *ApJ*, 816, 37
- Vestergaard, M. & Osmer, P. S. 2009, *ApJ*, 699, 800
- Vestergaard, M. & Wilkes, B. J. 2001, *ApJS*, 134, 1
- Vietri, G., Mainieri, V., Kakkad, D., et al. 2020, *A&A*, 644, A175
- Vietri, G., Piconcelli, E., Bischetti, M., et al. 2018, *A&A*, 617, A81
- Vito, F., Brandt, W. N., Bauer, F. E., et al. 2019a, *A&A*, 630, A118
- Vito, F., Brandt, W. N., Bauer, F. E., et al. 2019b, *A&A*, 628, L6
- Vito, F., Brandt, W. N., Luo, B., et al. 2018a, *MNRAS*, 479, 5335
- Vito, F., Brandt, W. N., Stern, D., et al. 2018b, *MNRAS*, 474, 4528
- Wang, F., Fan, X., Yang, J., et al. 2021a, *ApJ*, 908, 53
- Wang, F., Yang, J., Fan, X., et al. 2021b, *ApJ*, 907, L1
- Weisskopf, M. C., Wu, K., Trimble, V., et al. 2007, *ApJ*, 657, 1026
- Willott, C. J., Bergeron, J., & Omont, A. 2017, *ApJ*, 850, 108
- Woods, T. E., Agarwal, B., Bromm, V., et al. 2019, *PASA*, 36, e027
- Wu, X.-B., Wang, F., Fan, X., et al. 2015, *Nature*, 518, 512
- Yang, J., Wang, F., Fan, X., et al. 2020, *ApJ*, 897, L14
- Yi, W., Vivek, M., Brandt, W. N., et al. 2019, *ApJ*, 870, L25
- Zappacosta, L., Piconcelli, E., Giustini, M., et al. 2020, *A&A*, 635, L5

¹⁰ <http://www.astropy.org>